Supplemental Figures

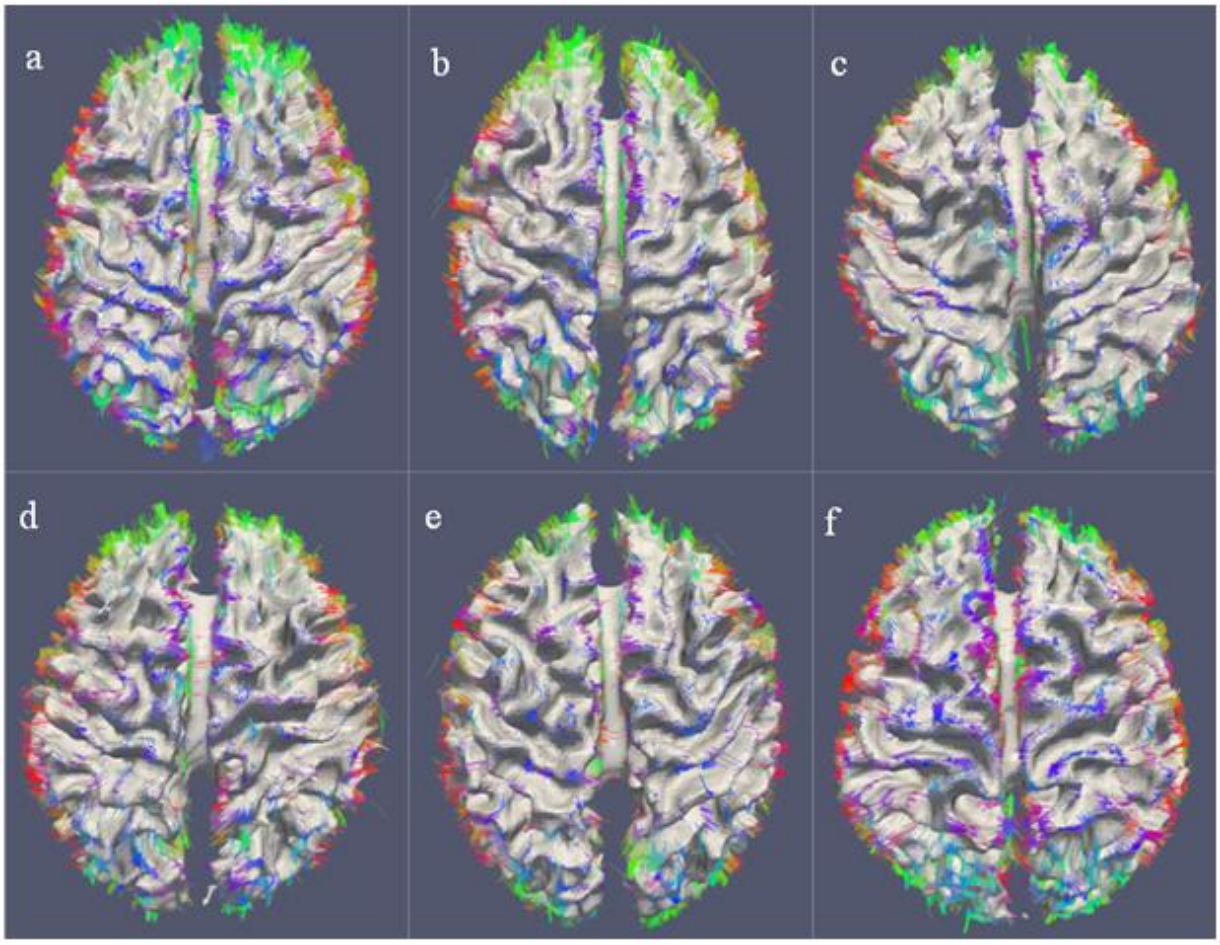

Supplemental Figure 1. (a)-(f): six additional cases of Fig. 1b.

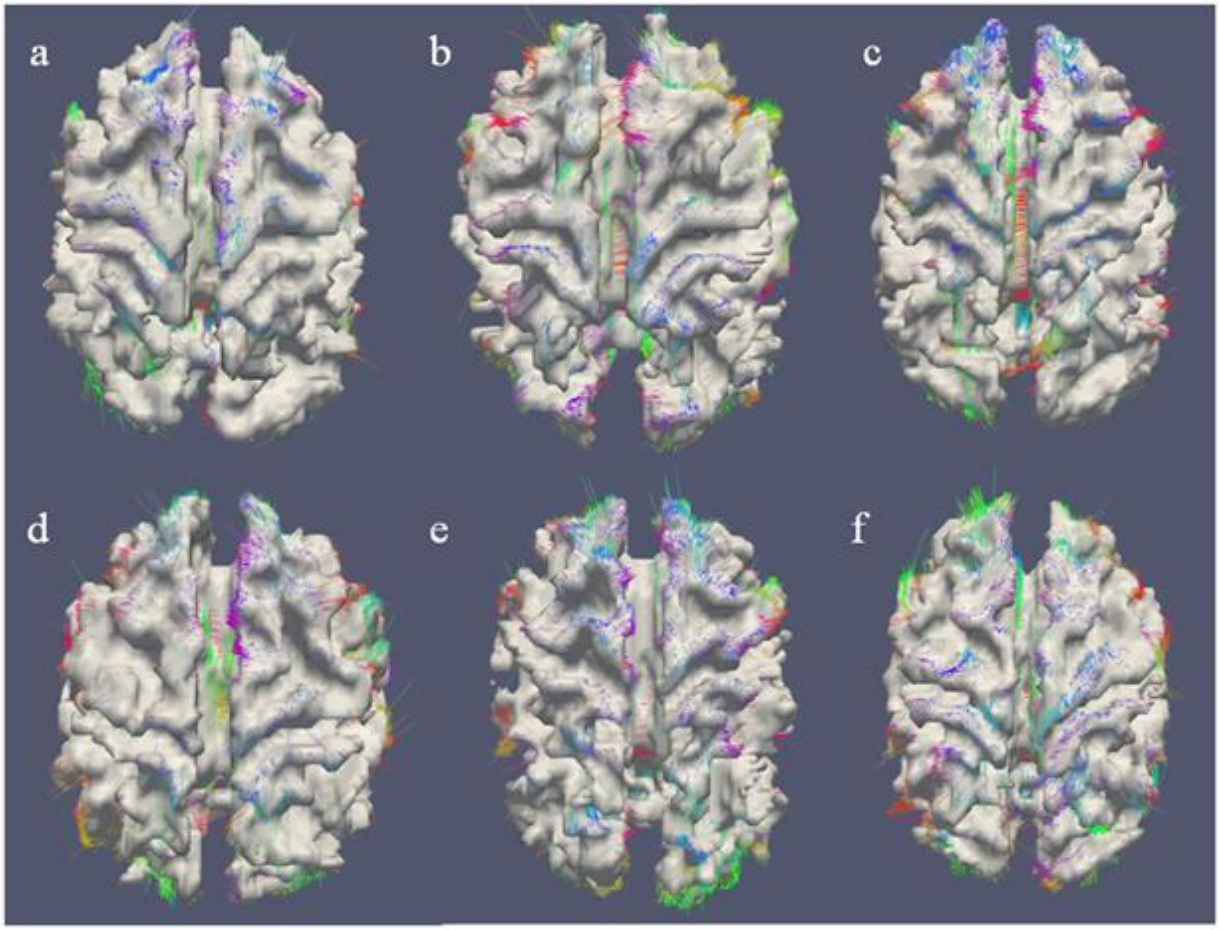

Supplemental Figure 2. (a)-(f): six additional cases of Fig. 2a.

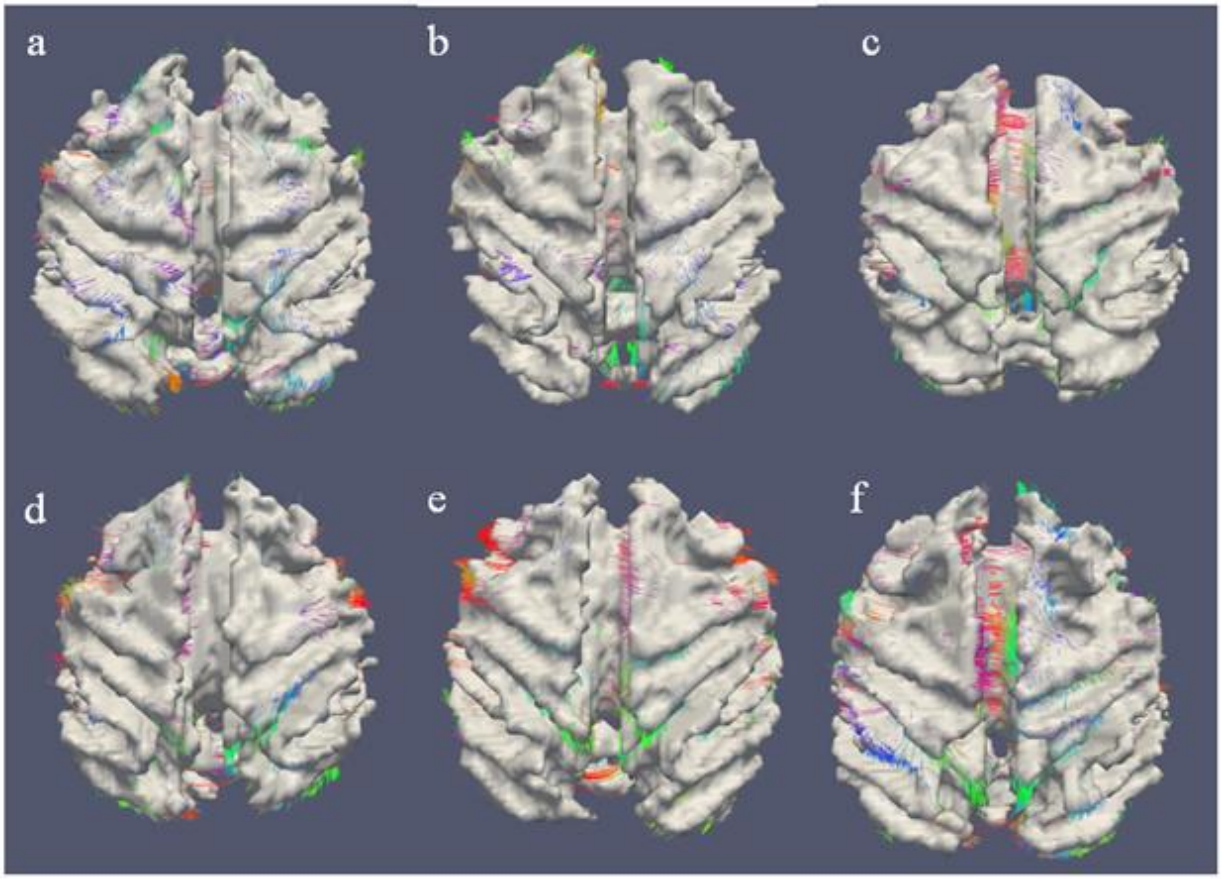

Supplemental Figure 3. (a)-(f): six additional cases of Fig. 2d.

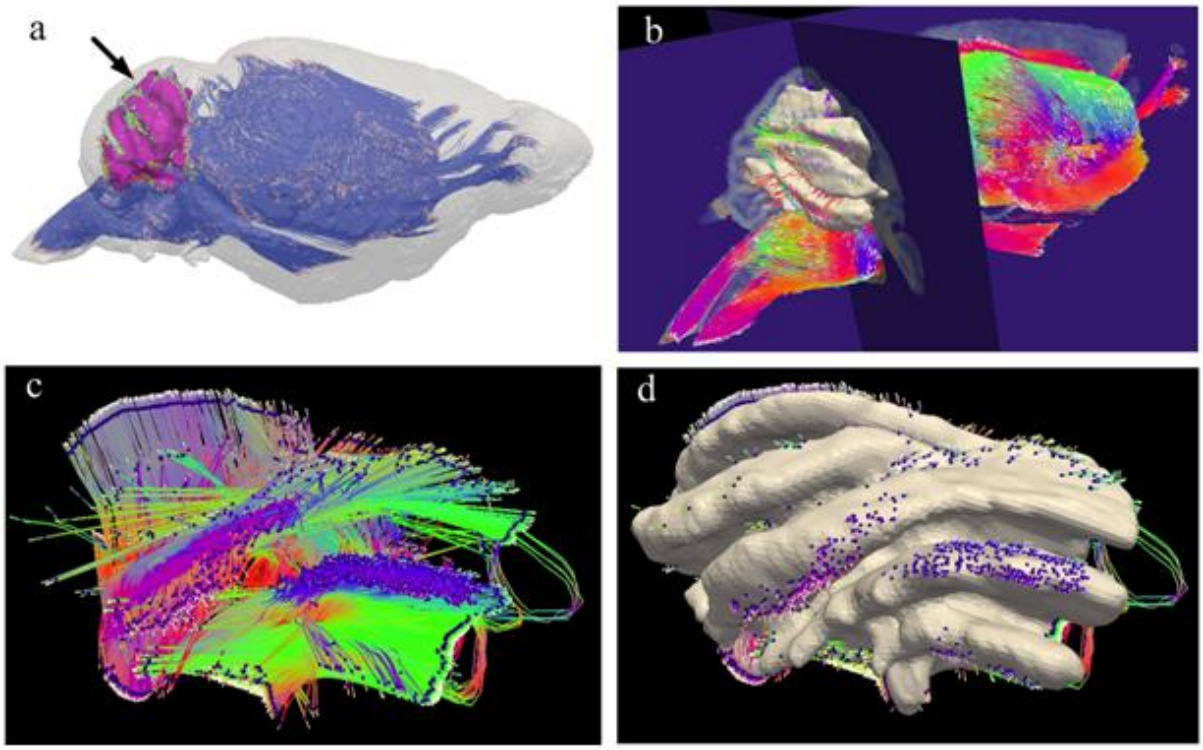

Supplemental Figure 4. Distributions of fiber end points concentrate on gyral regions in mouse cerebellum. (a): Joint visualization of axonal fibers and mouse brain. The purple region highlighted by the black arrow contains segmented gyri and sulci from the volumetric slices shown in (b). (b): Joint visualization of volumetric slices and axonal fibers. (c): Separate visualization of fibers within the purple region in (a) and their end points (blue dots). (d): Joint visualization of fibers and gyral surface within the purple region in (a). It is evident from (c) and (d) that most of end points of fibers are located in convex gyral regions in the mouse cerebellum.

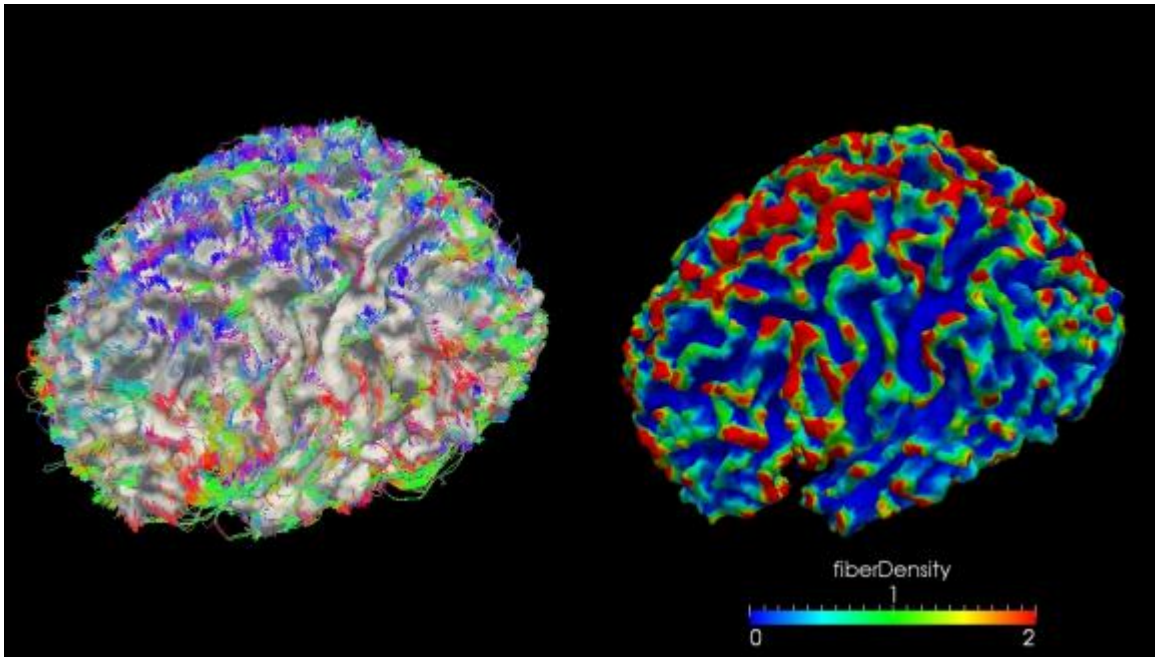
fiberDensity
1
0
2

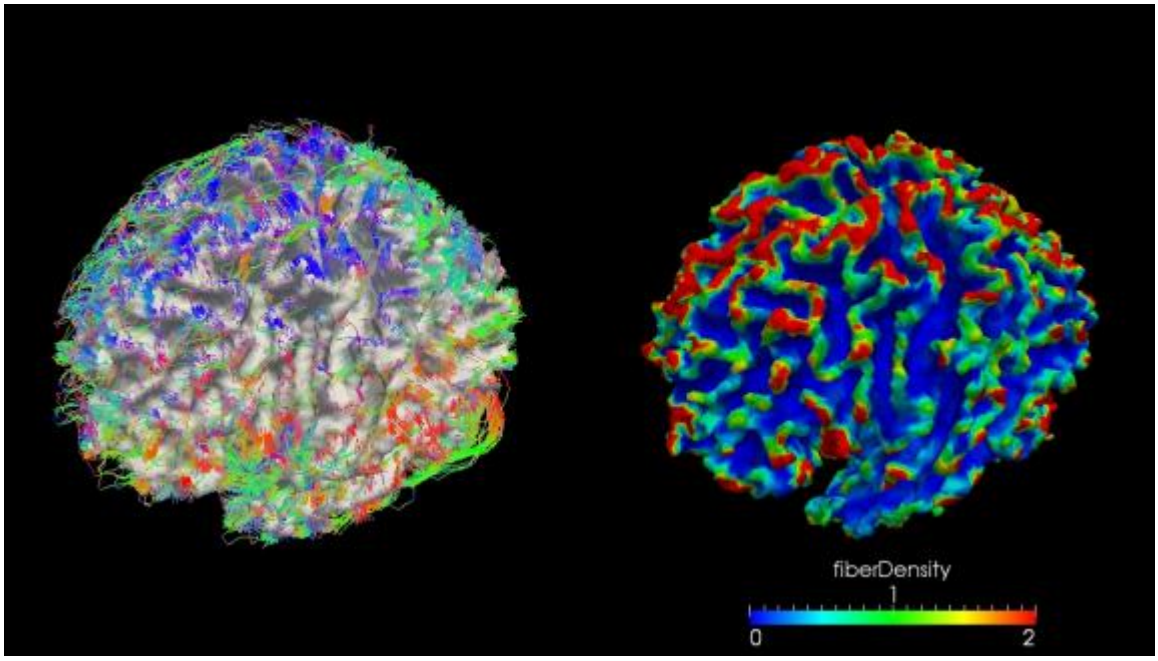
fiberDensity
1
0
2

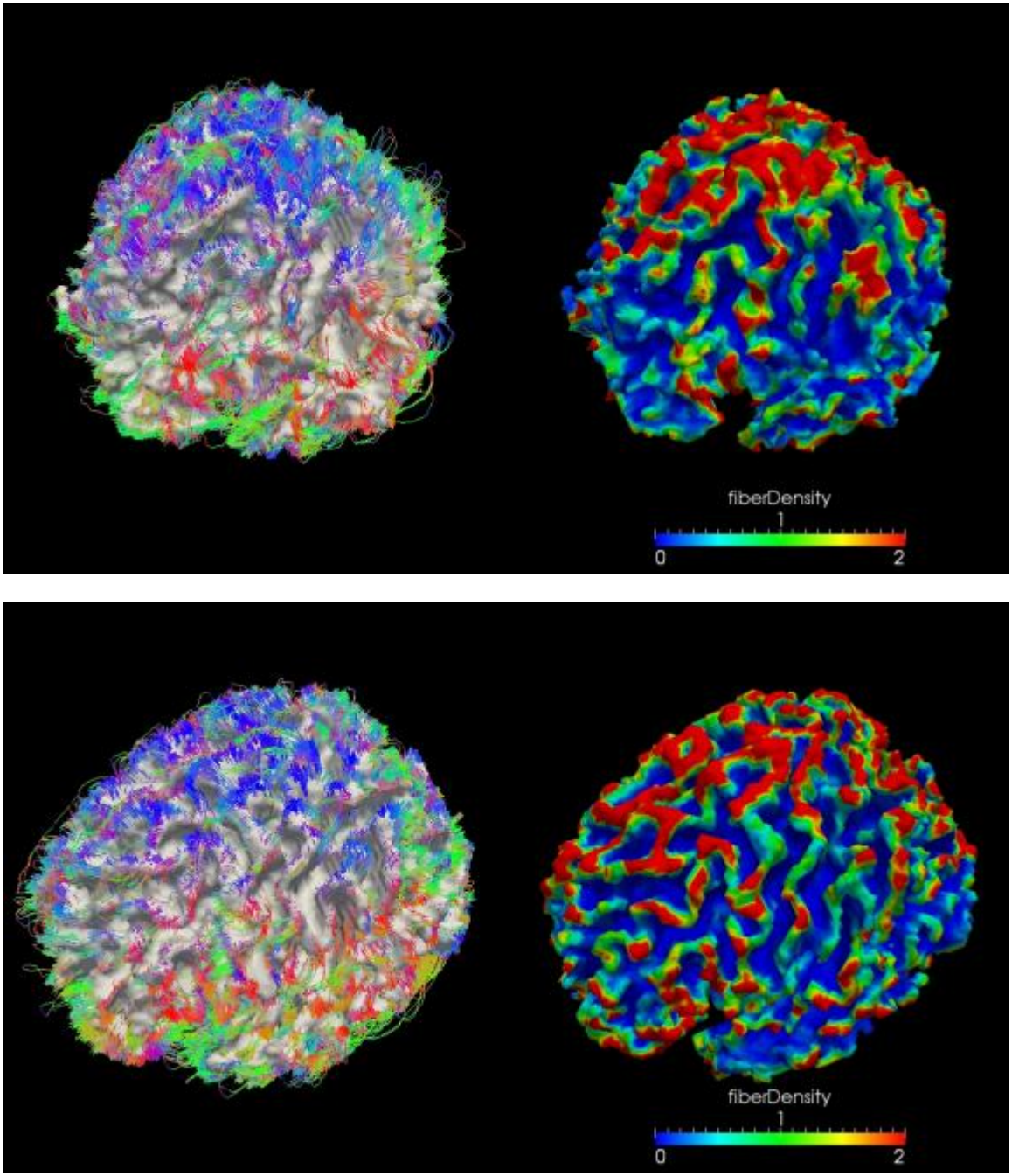

Supplemental Figure 5. Results of additional 4 HARDI cases. The annotations are the same as those in Fig. 3.

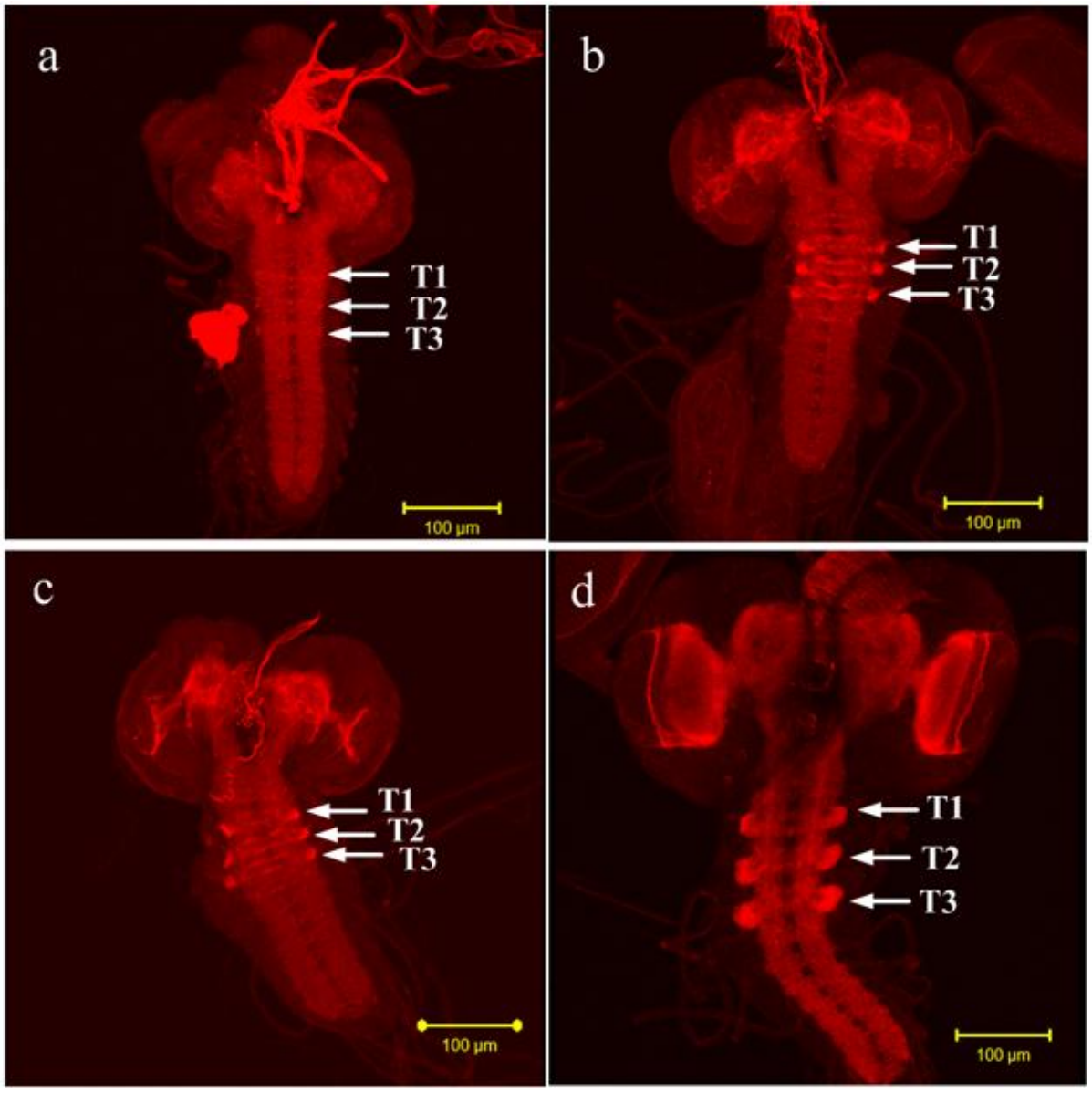

Supplemental Figure 6. (a)-(d): additional cases of Figs. 6a-6d. Annotations are the same as those in Fig. 6. (a): 72 hrs AED (after egg deposition); (b): 84 hrs AED, (c): 96 hrs AED; (d): 108 hrs AED.

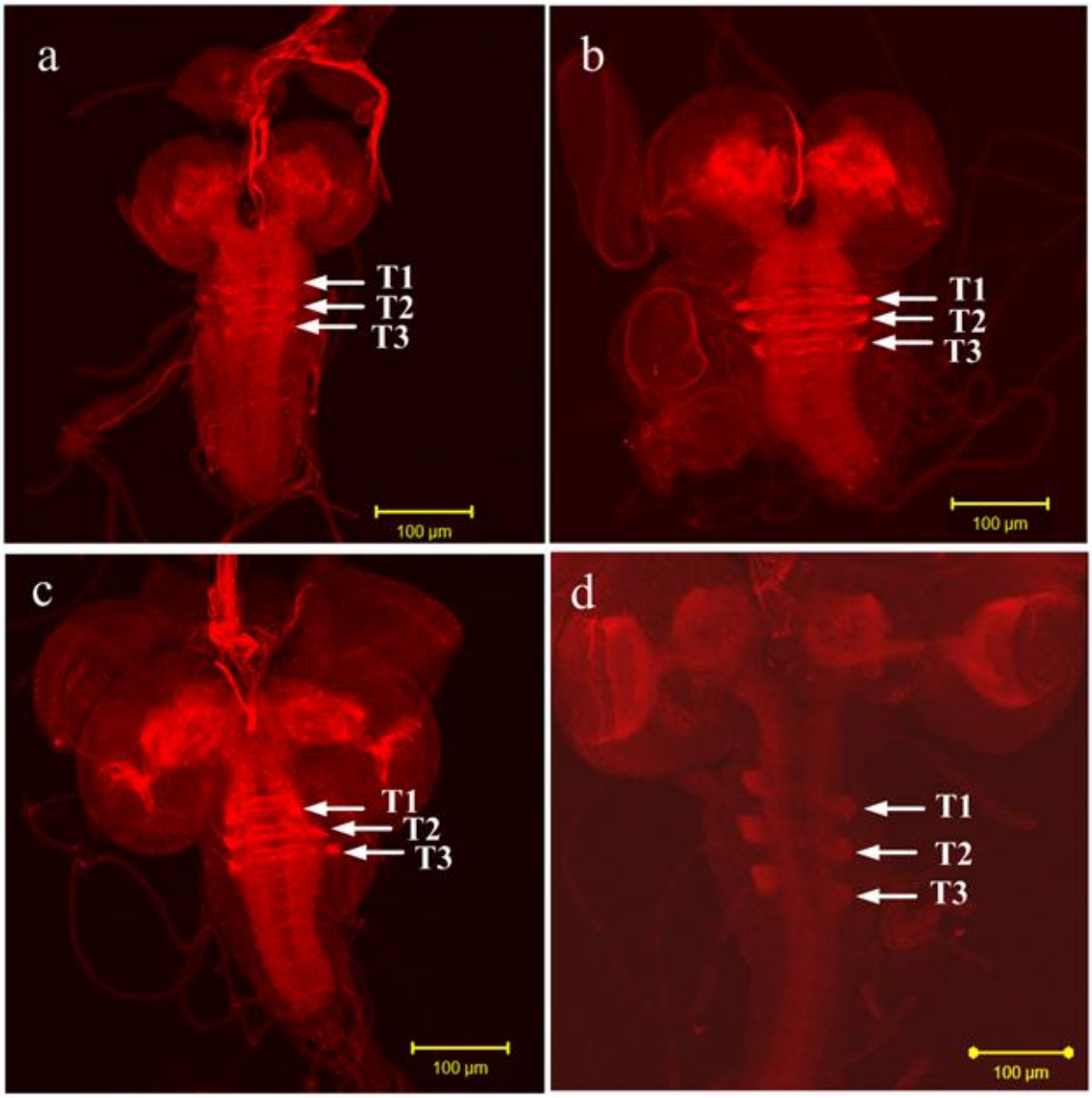

Supplemental Figure 7. (a)-(d): additional cases of Figs. 6a-6d. Annotations are the same as those in Fig. 6. (a): 72 hrs AED (after egg deposition); (b): 84 hrs AED, (c): 96 hrs AED; (d): 108 hrs AED.

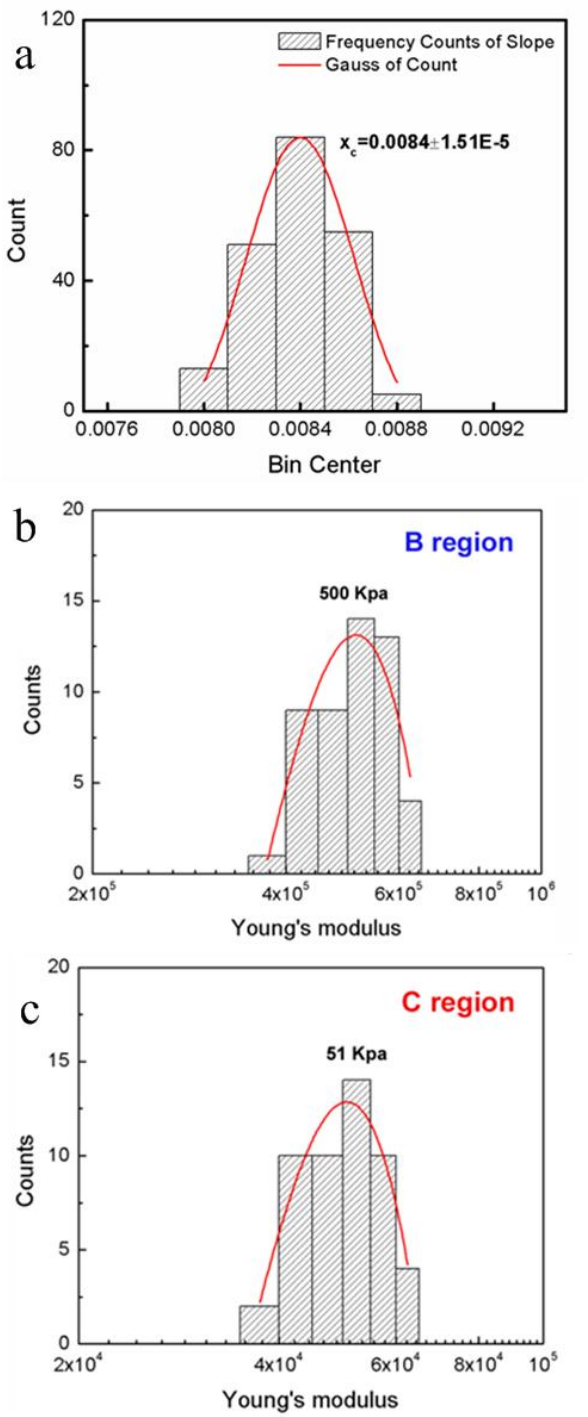

Supplemental Figure 8. AFM measurements of biomechanical properties of convex and concave regions in Drosophila thorax. (a): Histogram of sensitivities with center value of 0.0084 v/nm. The AFM deflection value in volt was transferred into the quantity in nm. (b): Histogram of

Young’s modulus measured at different points in B region (Center value: 500 Kpa). (c): Histogram of Young’s modulus measured at different points in C region (Center value: 51 Kpa).

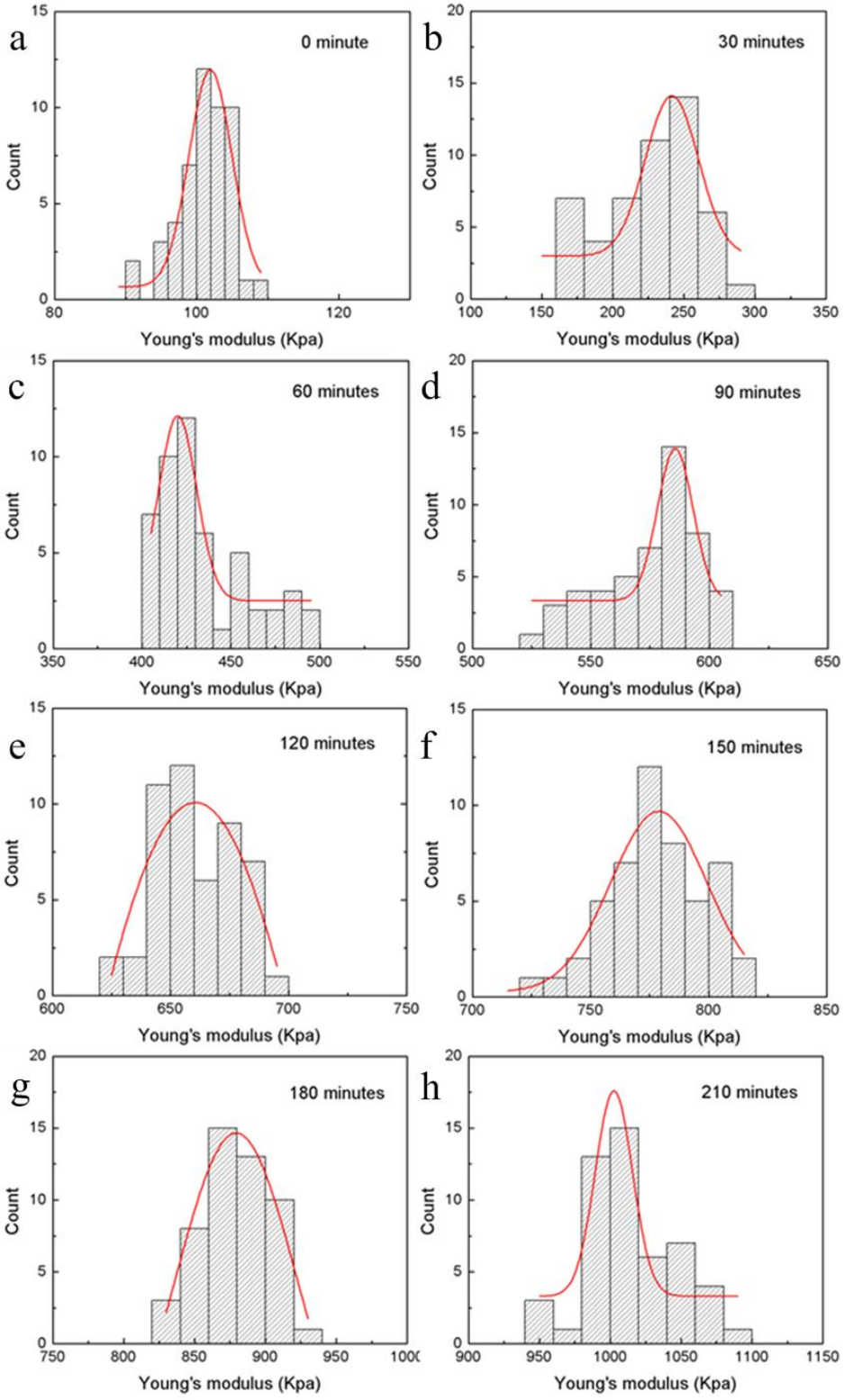

Supplemental Figure 9. (a)-(h): Histograms of Young's modulus measurements in different time points (0, 30, 60, 90, 120, 150, 180 and 210 minutes) during Drosophila development.

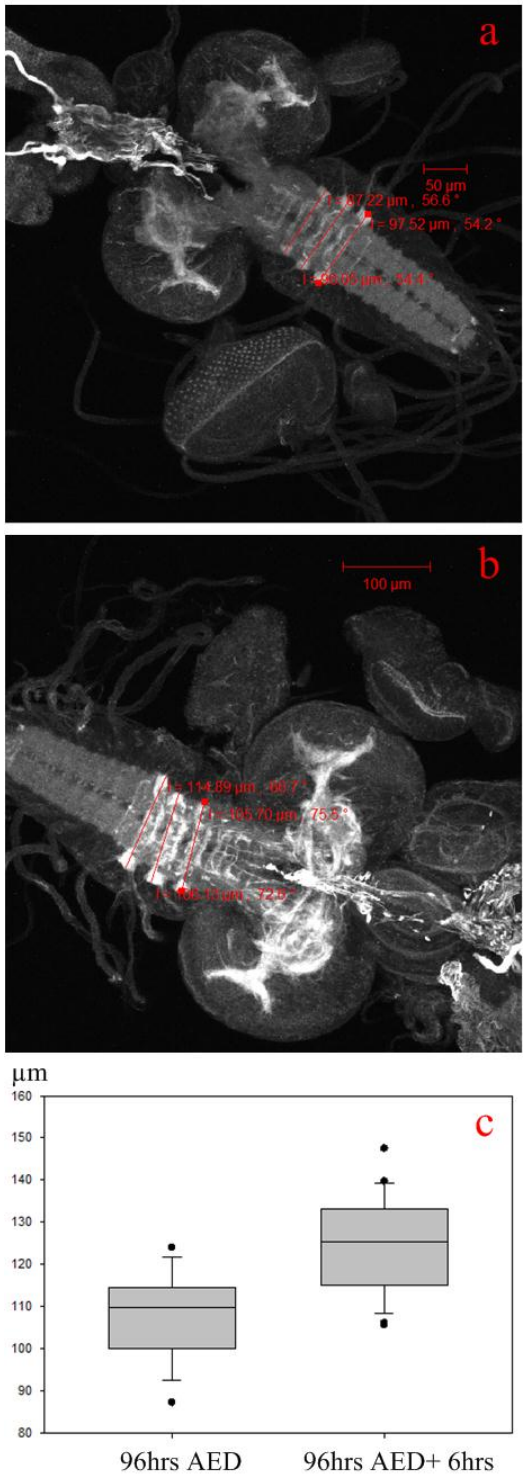

Supplemental Figure 10. Evidence showing that Drosophila under AFM imaging was live and can grow during the cultured window. (a): Length measurement of thorax in 96 hrs AED. (b): Length measurement of thorax in 102 hrs AED. (c): Statistics of thorax lengthens for fifteen

cases in time point 96 hrs and twenty four cases in time point 102 hrs. Mean and standard deviation were measured for each time point. It is evident that there is significant increase of the thorax length ($P = <0.001$) between the two time points.

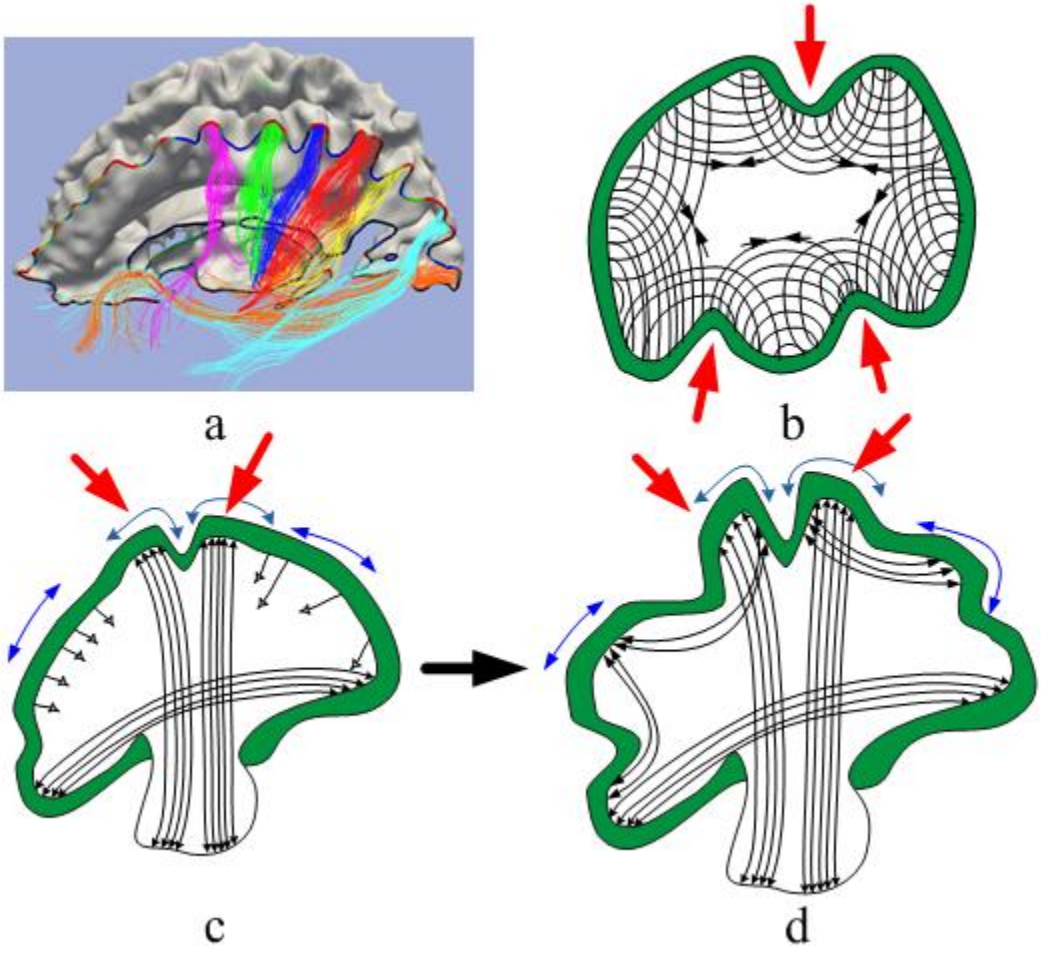

Supplemental Figure 11. Illustration of the tension-based morphogenesis (or axonal pulling) hypothesis (Van Essen 1997) and our axonal pushing hypothesis. (a): Illustrative visualization of the fact that dominant percentages of axonal fibers are connected to cortical gyral regions. Seven randomly colored fiber bundles are shown here. The gyral and sulcal curves are color-coded by red and blue, respectively. (b): Illustration of the axonal pulling hypothesis, implying that sulcal regions should have high density of axonal fibers, as illustrated by red arrows. (c): Stiff long-distance axonal fibers constantly "push" the cortical plate such that the cortical layers have to grow in the tangential directions. (d): More axons are wired into the brain networks and the cortical plate continues to grow into the convoluted gyral folds under the regulation of axonal pushing. The axonal pushing hypothesis implies that gyral regions should have high density of fibers, as illustrated by the red arrows in (c) and (d).

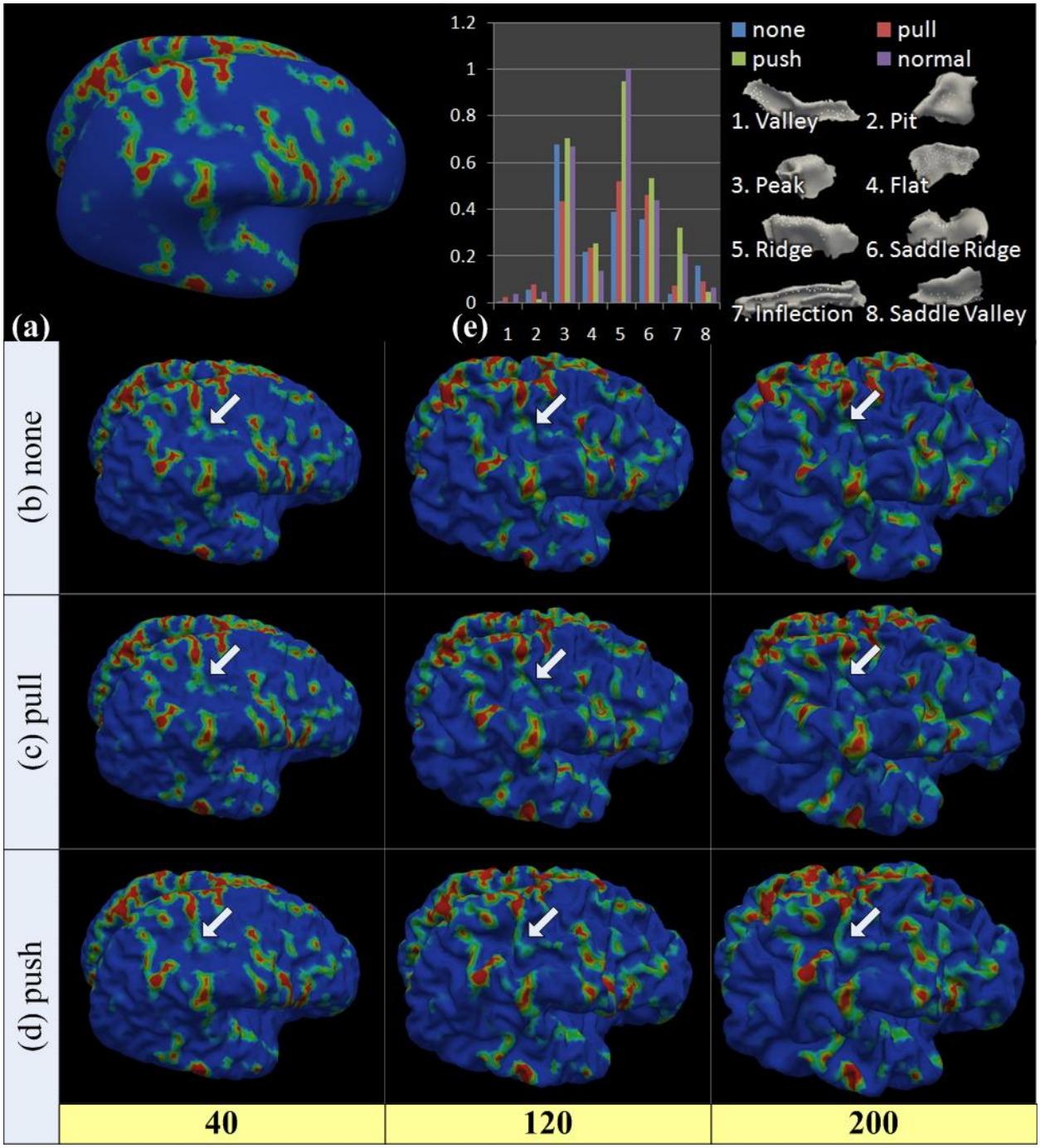

Supplemental Figure 12. Simulation results of computational models of cortical folding. (a): Synthesized fetus cortex via the in-house approaches (Chen et al., 2010). (b)-(d): Simulations obtained by no force, pulling and pushing force models, respectively. Simulation results at iteration 40, 120 and 200 are shown here. The white arrows highlight regions of significantly

better simulations by our axonal pushing model. (e): Comparison of fold shape patterns obtained by different simulation models with real-world cortical shapes patterns (represented by pink bars). The fold shape patterns are described by in-house tools (Zhang et al., 2009), and examples of eight shape patterns are also shown in (e).

Data acquisition and pre-processing

Human brain imaging dataset 1: Nine healthy young volunteers were scanned in a GE 3T Signa MRI system (GE Healthcare, Milwaukee, WI) using an 8-channel head coil at the Bioimaging Research Center (BIRC) of The University of Georgia, Athens, GA, under UGA IRB approval. Resting state fMRI (rsfMRI) data were acquired with dimensionality 128×128×60×100, spatial resolution 2mm×2mm×2mm, TR 5s, TE 25ms, and flip angle 90 degrees. DTI data were acquired using the same spatial resolution as the fMRI data; parameters were TR 15.5s and TE min-full, b-value = 1000 with 30 DWI gradient directions and 3 B0 volumes acquired. All scans were aligned to the AC-PC line.

Pre-processing of the rsfMRI data included brain skull removal, motion correction, spatial smoothing, temporal prewhitening, slice time correction, global drift removal, and band pass filtering (0.01Hz~0.1Hz). For the DTI data, pre-processing included brain skull removal, motion correction, and eddy current correction. After the pre-processing, fibers tracts, gray matter (GM) and white matter (WM) tissue segmentations (Liu et al., 2007), and the GM/WM cortical surface (Liu et al., 2008) were generated based on the DTI data. Fiber tracking was performed using MEDINRIA (http://www-sop.inria.fr/asclepios/software/MedINRIA/). Brain tissue segmentation was conducted on DTI data (Liu et al., 2007). Based on the WM, the cortical surface was reconstructed using the marching cubes algorithm. The reconstructed surface has about 40,000 vertices.

Human brain imaging dataset 2: Fifteen healthy university students were recruited to participate in this study under UGA IRB approval. DTI scans were acquired for each participant. FMRI and DTI scans were acquired on a GE 3T Signa scanner using an 8-channel head coil at the UGA BIRC. Acquisition parameters were as follows: fMRI: 64x64 matrix, 4mm slice thickness, 220mm FOV, 30 slices, TR=1.5s, TE=25ms, ASSET=2; DTI: 128×128 matrix, 2mm slice thickness, 256mm FOV, 60 slices, TR=15100ms, TE= min-full, ASSET=2, 3 B0 images, 30 optimized gradient directions, b-value=1000). All scans were aligned to the AC-PC line. The same pre-processing steps were performed on this dataset as the first.

Chimpanzees: MRI scans were obtained from 36 adult female chimpanzees. Fifteen cases were randomly selected for this study. All chimpanzees were members of a colony at Yerkes National Primate Research Center (YNPRC) in Atlanta, Georgia. We do not currently have access to a comparable set of MRI scans from male chimpanzees. All imaging studies were conducted at the YNPRC of Emory University under IRB approval.

Prior to scanning, the subjects were immobilized with ketamine injections (2−6 mg/kg, i.m.) and were subsequently anesthetized with an intravenous propofol drip (10 mg/kg/hr) following standard veterinary procedures used at YNPRC. The subjects remained sedated for the duration of the scans as well as the time needed for transport between their home cage and the scanner location. After completing the MRI scan, the chimpanzees were temporarily housed in a single cage for 6 to 12 hours to allow the effects of anesthesia to wear off before being returned to their home cage and cage mates. The veterinary staff and research staff observed the general well-

being (i.e., activity, food intake) of the chimpanzees twice daily after the scan for possible distress associated with aesthetic accesses.

Both anatomical and diffusion MRI scans were acquired on a Siemens 3T Trio scanner (Siemens Medical System, Malvern, PA) with a standard birdcage coil. Foam cushions and elastic straps were used to minimize head motion. High-resolution T1-weighted images were acquired with a 3D magnetization-prepared rapid gradient-echo (MPRAGE) sequence for all participants. The scan protocol, optimized at 3T, used a repetition time/inversion time/echo time of 2400/1100/4.13 msec, a flip angle of 8°, a volume of view of 256×256×154 mm, a matrix of 256×256×192, and resolution of 1.0×1.0×0.8 mm, with 2 averages. Total T1 scan time was approximately 20 minutes.

Diffusion MRI data were collected with a diffusion-weighted, multi-shot (four segments), spin-echo echo planar imaging (EPI) sequence. A dual spin-echo technique combined with bipolar gradients was used to minimize eddy-current effects. The parameters used for diffusion data acquisition were as follows: diffusion-weighting gradients applied in 60 directions with a b value of 1000 sec/mm^2; repetition time/echo time of 5740/91 msec, field of view of 230×230 mm^2, matrix size of 128×128, resolution of 1.8×1.8×1.8 mm, 41 slices with no gap, covering the whole brain. Averages of two sets of diffusion-weighted images with phase-encoding directions of opposite polarity (left – right) were acquired to correct for susceptibility distortion. For each average of diffusion-weighted images, six images without diffusion weighting (b=0 sec/mm^2) were also acquired with matching imaging parameters. The total diffusion MRI scan time was

approximately 50 minutes. Pre-processing steps were similar to those used in process of human DTI data.

Macaques: MRI scans were obtained from 25 adult female macaques. Fifteen cases were randomly selected for this study. All macaques were members of a colony at Yerkes National Primate Research Center (YNPRC) in Atlanta, Georgia. We do not currently have access to a comparable set of MRI scans from male macaques. All MRI and DTI scans were conducted at the YNPRC of Emory University under IRB approval.

Prior to scanning, the subjects were immobilized with ketamine injections (2−6 mg/kg, i.m.) and were subsequently anesthetized with an intravenous propofol drip (10 mg/kg/hr) following standard veterinary procedures used at YNPRC. The subjects remained sedated for the duration of the scans as well as the time needed for transport between their home cage and the scanner location. After completing the MRI scan, the macaques were temporarily housed in a single cage for 6 to 12 hours to allow the effects of anesthesia to wear off before being returned to their home cage and cage mates. The veterinary staff and research staff observed the general well-being (i.e., activity, food intake) of the macaques twice daily after the scan for possible distress associated with anaesthetic accesses.

Both anatomical and diffusion MRI was performed on a Siemens 3T Trio scanner (Siemens Medical System, Malvern, PA) with a standard knee coil. Foam cushions and elastic straps were used to minimize head motion. A specially designed holding device was used to stabilize macaque's head during scanning, with two plastic screws pushing the macaque's ear canals

tightly. High-resolution T1-weighted images were acquired with a 3D magnetization-prepared rapid gradient-echo (MPRAGE) sequence for all participants. The scan protocol, optimized at 3T, used a repetition time/inversion time/echo time of 2500/950/3.49 msec, a flip angle of 8°, a volume of view of 128×128×96 mm^3, a matrix of 256×256×192, and resolution of 0.5×0.5×0.5 mm^3, with 3 averages. Total T1 scan time was approximately 33 minutes.

Diffusion MRI data were collected with a diffusion-weighted, multi-shot (three segments), spin-echo echo planar imaging (EPI) sequence. A dual spin-echo technique combined with bipolar gradients was used to minimize eddy-current effects. The parameters used for diffusion data acquisition were as follows: diffusion-weighting gradients applied in 60 directions with a b value of 1000 sec/mm^2; repetition time/echo time of 6970/104 msec, field of view of 141×141 mm^2, matrix size of 128×128, resolution of 1.1×1.1×1.1 mm, 41 slices with no gap, covering the whole brain. Averages of four sets of diffusion-weighted images with phase-encoding directions of opposite polarity (left – right) were acquired to correct for susceptibility distortion. For each average of diffusion-weighted images, five images without diffusion weighting (b=0 sec/mm^2) were also acquired with matching imaging parameters. The total diffusion MRI scan time was approximately 90 minutes. Pre-processing steps were similar to those used in process of human DTI data.

Mouse: High resolution diffusion tensor microimaging data (45 micron per pixel isotropic) of embryonic mouse brain was downloaded from the Mouse BIRN Data Repository (http://www.birncommunity.org/data-catalog/mouse-diffusion-tensor-imaging-dti-atlas-of-developing-mouse-brains).

Drosophila: The fly stocks used in the experiments were Drosophila melanogaster. All flies were raised at 25°C unless otherwise indicated. w1118 flies were used as wild type. The CNS of different developmental stages was dissected in PBS, fixed in 4% formaldehyde for 40 minutes following 5 times washing of PBT (PBS+0.3 % Tx-100). Incubation with Rhodamine phalloidin (Cytoskeleton, Cat. #PHDR1, 1:200 dilution) was carried out at 4°C overnight. The Actin was stained by rhodamine conjugated phalloidin. Fluorescent images were collected by Zeiss LSM 510 Meta Confocal Microscope and processed by the NIH Image J program (http://rsbweb.nih.gov/ij/).

AFM imaging: Fresh Drosophila tissue was dissected for each experiment. Further it was immediately transferred and immobilized on a glass cover-slip with poly-lysine coating. To keep the dissected tissue temporarily alive as long as possible, it was stored and imaged under HyQ tissue culture media. With the aid of an optical microscope, the AFM probe was located directly above the interested place. Contact mode imaging was carried out in Agilent 5500 AFM using multi-purpose AFM scanner with scanning range of 10 μm2 and the silicon nitride probe with nominal spring constant of 0.006 N/m (Budget sensor).

Force versus distance curves were measured at specific positions of the Drosophila thorax identified after AFM imaging. To acquire faithful values of Young's modulus at the specific areas, the maximum force load was controlled from 1000 pN to 3000 pN, and the indentation frequency was varied from 0.1 to 1 Hz. Since only the relative magnitude of Young's modulus

was the main concern of our study, all the nominal physical properties of the AFM probe were applied here without re-calibration.

There are several kinds of Hertz models for the probes with different geometries. Since the manufacturer of the AFM probe describes its geometry as a sharp cone, the Hertz model for a conical tip was adopted here.

$$z - z_0 = d - d_0 + \sqrt{\frac{k(d - d_0)}{(2/\pi)[E(1 - \nu^2)]\tan(\alpha)}}$$

where z is the piezo movement, z_0 is the contact point, d is the deflection of the cantilever, d_0 is the zero deflection which could be determined in the noncontact part of the force curve, k is the spring constant, E is the elastic or Young's modulus, υ is the Poisson ratio which is assumed to be 0.5, and α is the half opening angle of the indenting cone. The two unknown quantities, z_0 and E, can be determined by fitting contact part of the force curve with Hertz model. This analysis work was done by in-house software based on Labview.

Computational modelling methods

Computational simulation of cortical folding: Cortical folding simulations were based on our recently developed simulation framework (Nie et al., 2010). Briefly, the computational framework is composed of four key components: 1) A deformable model of the cortex. This model provides a geometric representation of the cortex that can be deformed into dynamic shapes via mechanical forces. 2) Forces driving the folding. The mechanical driving forces that are inferred from the cortical growth model deform the cortical surface under partial differential

equations. 3) Geometric constraints. Cortical growth is constrained by the brain skull and boundary conditions. 4) Model solvers. The numerical solution to the partial differential equations guides the dynamic evolution of the geometric surface model of the cortex.

In this work, additional axonal pulling or pushing forces were added to drive the deformation of the geometric model as follows.

(1) Pulling model. This model is defined according to the tension-based theory of morphogenesis (Van Essen, 1997) where the pulling forces exist at the ends of axons. When the cortex is deforming outward, fiber connections will generate an inward pulling force on the cortical vertex. According to literature reports (Dennerll et al., 1989; Steven et al., 1997), developing axons in the CNS can be described as Newtonian fluid mechanical elements, so the strength of pulling force is in direct proportion to outgrowth velocity. Thus, the pulling force on the cortical vertex is defined as:

$$\mathbf{F}_{pull}^{i} = -\kappa_{pull} D_{fib}^{i} \cdot \mathbf{v}^{i}$$

where i is the vertical index, κ_{pull} controls the fiber strength, D_{fib}^{i} is the fiber density and $\mathbf{v}^{i}$ is the deforming speed of the vertex.

(2) Pushing model. This model is based on the hypothesis that cortical regions with high fiber density will be much stiffer, and thus the inward bending of cortex region becomes slow-down. When the growing cortical vertex is bending inward, a pushing force will be generated by the stiffness of the fiber:

$$\mathbf{F}_{stiff}^{i} = \begin{cases} 0 & \mathbf{v}^{i} \cdot \mathbf{n}^{i} \geq 0 \\ \kappa_{stiff} D_{fib}^{i} \cdot \mathbf{n}^{i} & \mathbf{v}^{i} \cdot \mathbf{n}^{i} < 0 \end{cases}$$

where i is the vertical index, κ_{stiff} is the stiffness parameter, D_{fib}^{i} is the fiber density, $\mathbf{n}^{i}$ is the normal direction of vertex and $\mathbf{v}^{i}$ is the deforming speed of the vertex. As a result, $\mathbf{F}_{stiff}^{i}$ will be generated when the cortical vertex is deforming inward.

In this paper, three conditions were investigated in our simulations: a) there is no axonal pulling or pushing force; b) there is an axonal pulling force based on the tension-based morphogenesis theory (Van Essen, 1997); and c) there is a pushing force as we proposed. Initial fetus cortex was synthesized via in-house approaches (Chen et al., 2010). Simulation results are in Supplemental Fig. 12.

Supplemental References:

Chen H., Guo L., Nie J., Zhang T., Hu X., Liu T., (2010) A dynamic skull model for simulation of cerebral cortex folding, Proceedings of Medical Image Computing and Computer Assisted Intervention, 13(Pt 2):412-419.

Dennerll T. J., Lamoureux P., Buxhaum R. E., Heidemann S.R. 1989. The cytomechanics of axonal elongation and retraction, J. Cell Biol., 109:3073~3083.

Li K., Guo L., Li G., Nie J., Faraco C., Zhao Q., Miller L., Liu T., 2010. Cortical surface based identification of brain networks using high spatial resolution resting state fMRI data, Proceedings of International Symposium of Biomedical Imaging, 656 – 659.

Nie J., Guo L., Li G., Faraco C., Miller L. S., Liu T., (2010) A computational model of cerebral cortex folding, Journal of Theoretical Biology, 264(2):467-78.

Liu T., Li H., Wong K., Tarokh A., Guo L., Wong S. 2007. Brain Tissue Segmentation Based on DTI Data, NeuroImage, 38(1):114-23.

Liu T., Nie J., Tarokh A., Guo L., Wong S. 2008. Reconstruction of Central Cortical Surface from MRI Brain Images: Method and Application. NeuroImage, 40(3):991-1002.

Steven R. Heidemann, Phillip Lamoureux, R. E. Buxbaum, 1997. Cytomechanics of Axonal Development, Cell Biochemistry and Biophysics, 27:135~155.

Van Essen D.C. 1997. A tension-based theory of morphogenesis and compact wiring in the central nervous system. Nature. 385:313-318.

Zhang T., Guo L., Li G., Nie J., Liu T., (2009) Parametric representation of cortical surface folding via polynomials, Proceedings of Medical Image Computing and Computer Assisted Intervention (MICCAI), 5762:184–191.